


The effects of the core material (M = Co, Ni) and catalyst support (N = MWCNTs and rGO) on the performance of M@Pd/N core-shell electrocatalysts for formate oxidation and direct formate-hydrogen peroxide fuel cells †

 Author and affiliation details can be edited in the panel that appears to the right when you click on the author list.

Raana Mahmoodi^a, Mir Ghasem Hosseini,^(iD 0000-0002-3117-8608)(B-2950-2011)^{a,b,c,*}, Saeid Abrar^a and Richard J. Nichols,^(iD 0000-0002-1446-8275)(H-2157-2015)^d


^aDepartment of Physical Chemistry, Electrochemistry Research Laboratory, University of Tabriz, Tabriz, Iran, mg-hosseini@tabrizu.ac.ir, +9841333340191, +9841333393138

^bEngineering Faculty, Department of Materials Science and Nanotechnology, Near East University, 99138 Nicosia, North Cyprus, Mersin 10, Turkey

^cElectrochemistry Research Center of Production and Stages Energy, University of Tabriz, Tabriz, Iran

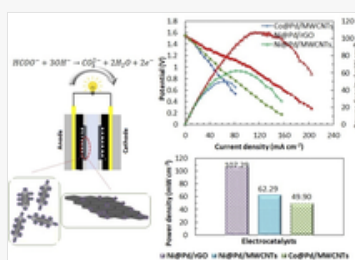
^dDepartment of Chemistry, Donnan and Robert Robinson Laboratories, University of Liverpool, Liverpool L69 7ZD, UK

Funding Information

 We have combined the funding information you gave us on submission with the information in your acknowledgements. This will help ensure the funding information is as complete as possible and matches funders listed in the Crossref Funder Registry. Please check that the funder names and award numbers are correct. For more information on acknowledging funders, visit our website: <http://www.rsc.org/journals-books-databases/journal-authors-reviewers/author-responsibilities/#funding>.

Funder Name :	Iran National Science Foundation
Funder's main country of origin :	
Funder ID :	10.13039/501100003968
Award/grant Number :	97018389

Table of Contents Entry



The obtained results show that the presence of Ni at the core instead of Co improved the catalytic performance of the M@Pd/MWCNTs catalyst due to the synergistic effects between Ni and Pd, and also that Ni@Pd/rGO performed better for formate oxidation because of the high surface area of rGO with respect to MWCNTs. The obtained results show that the presence of Ni at the core instead of Co and using rGO as catalyst support instead of MWCNTs increased the catalytic performance of the synthesized electrocatalyst towards formate oxidation.

Abstract

In this work, M@Pd/N (M = cobalt, nickel; N = multi-walled carbon nanotube, reduced graphene oxide) anodic electrocatalysts are synthesized and studied for formate oxidation, and used directly in formate-hydrogen peroxide fuel cells (DFHPFCs) for the first time. The effect of core materials (M = cobalt, nickel) on the activity of M@Pd/MWCNTs for formate oxidation has been studied. For this purpose, a Co@Pd/MWCNT electrocatalyst is synthesized using a two-step reduction method. Comparing the electrochemical surface area (ECSA), the formate oxidation current density (I_p) and onset potential of formate oxidation (E_{ons}) values of Co@Pd/MWCNTs and Ni@Pd/MWCNTs showed that the presence of Ni in the core instead of Co improved the catalytic performance of the M@Pd/MWCNT catalyst due to the synergistic effects between Ni and Pd. The ECSA and I_p values of the Ni@Pd/MWCNTs are 1.01 and 1.78 times higher than those of Co@Pd/MWCNTs. After optimizing the core material, in the next step, the effect of the catalyst support on the performance of Ni@Pd nanoparticles is evaluated. Comparing the ECSA, I_p and E_{ons} values of Ni@Pd/MWCNTs and Ni@Pd/rGO showed that Ni@Pd/rGO performs better for formate oxidation because of the high surface area and conductivity of rGO compared to MWCNTs. The ECSA and I_p values of Ni@Pd/rGO are 1.09 and 1.57 times higher than those on Ni@Pd/MWCNTs. Finally, the effect of these electrocatalysts in DFHPFC is evaluated and the results are in good agreement with the three electrode results. The maximum power density of the Co@Pd/MWCNTs, Ni@Pd/MWCNTs and Ni@Pd/rGO is 49.90, 62.29 and 107.29 mW cm^{-2} , respectively.

1. Introduction

Increasing energy demand, on the one hand, and declining fossil fuel resources, along with rising greenhouse gas concentrations, on the other hand, have prompted researchers to look for renewable energy sources.¹⁻³ Fuel cells can achieve minimal pollution and very low emissions of greenhouse or polluting gases (such as CO_2 , NO_x , and SO_x , etc.). Higher energy density and energy efficiencies are desired from fuel cells if they are to replace conventional systems, which presents challenges for both engineers and scientists.^{4,5} Fuel cells are promising electrochemical devices, which are able to convert chemical energies of fuel (methanol, hydrogen), in the presence of a catalyst and with pure oxygen or air as the oxidant, into electrical energy, heat and water. The advantages of fuel cells include the following: (1) the fuel cell generates electricity directly from chemical energy, so it could be more efficient, (2) the components and structure of most fuel cells offer constructional and mechanical benefits, since fuel cells have no or minimal moving components, making fuel cells noiseless catalysts. This attribute means that fuel cells can have a long life, depending on durability. (3) Certain fuel cell types have potentially higher energy densities than batteries and can be fed quickly, while batteries must either be discarded or recharged after a while.^{6,7}

Polymer electrolyte membrane fuel cells (PEMFCs) that work with liquid fuels instead of hydrogen as the traditional fuel offer attractive attributes. Due to problems related to the transportation and storage of hydrogen gas,⁸ other hydrogen-rich liquid fuels such as methanol,⁹⁻¹¹ hydrazine,¹² sodium borohydride,¹³⁻¹⁵ and formate¹⁶ can also be used in PEMFCs. These types of polymer electrolyte membrane fuel cells are called direct liquid fuel cells (DLFCs) due to their use of liquid fuels. Among the different types of liquid fuels, formates have recently attracted a lot of consideration.¹⁷⁻²⁰ The advantages of formate compared to other liquid fuels include the following: (1) formate could act as a carbon neutral fuel if, for example, it is obtained by reducing carbon dioxide by artificial photosynthesis,^{17,18} (2) oxidation of formate is rapid in alkaline media, especially on palladium particles,¹⁹ (3) the open circuit potential of the formate fuel cell in the presence of oxygen/air as the oxidant is about 1.45 V, which is 0.24 V and 0.31 V more than the potential of methanol and ethanol fuel cells, respectively.²¹ (4) In contrast to the acidic environment, there are no toxic effects of the oxidation of formate in alkaline environments,²⁰ and (5) solid formate salts are easily transported

and stored, and are highly soluble in water for yielding liquid fuel.²² Therefore, numerous efforts have been made to develop direct-formate fuel cells.^{23,24}

Electrocatalysts used in DLFCs have a major effect on the performance of fuel cells. The two main components of an electrocatalyst are the metal nanoparticles and the catalyst substrate on which these metal nanoparticles are deposited. Palladium-based catalysts have the highest catalytic activity with respect to formate oxidation in both acidic and alkaline media.²⁵ Also, formate does not cause palladium poisoning.²⁶ An effective way to reduce the consumption of the precious metal (palladium) and increase its catalytic activity is to alloy palladium with oxyphilic transition metals to help oxidize the adsorbed carbon monoxide species and reduce the poisoning of the catalyst.^{27,28} Furthermore, the synthesis of catalytic nanoparticles with a core-shell structure can increase the electrocatalyst activity compared to the alloy structure with the same amount of metal loading. This is because, in the core-shell structure, the precious metal with high catalytic performance for formate oxidation is placed on the outer surface of the nanoparticles (shell) and so is in more direct contact with the formate solution than when inside the nanoparticle core.²⁹ For instance, Wang *et al.* synthesized the Pt@Ru core shell nanoparticles and used them as an anodic electrocatalyst for methanol oxidation in a direct methanol fuel cell (DMFC). They concluded that by using Pt@Ru with a core-shell structure, the power density of DMFC was increased to 93 mW cm^{-2} compared to the PtRu with an alloy structure (35 mW cm^{-2}).³⁰ In another study, Sohail *et al.* evaluated the catalytic activity of the PtCo/MWCNTs with alloy and core-shell structures for methanol oxidation. Electrochemical investigations showed that the methanol oxidation current density on the core-shell structure is 1.6 times higher than that on the catalyst with an alloy structure.³¹ Also, Zhao *et al.* concluded that the Ni@Pd/MWCNTs perform better for methanol oxidation than the alloy structure.³² In our previous work, we showed that Ni@Pt/C has a higher activity for borohydride oxidation than NiPt/C with an alloy structure.²⁹

The other part of the electrocatalyst that has a great influence on its performance is the catalyst substrate on which the nanoparticles are dispersed.³³ Different supports (such as vulcan, multi-walled carbon nanotubes, and reduced graphene oxide) have been used in fuel cell studies. Carbon nanotubes, a carbon allotrope, were discovered in 1991 and consist of hollow cylinders composed of graphite layers and sp^2 bonding similar to graphite. The bonding patterns give a stable structure and extraordinary mechanical strength. Another carbon allotrope is graphene.³⁴ Graphene is a monolayer of carbon atoms with a two-dimensional hexagonal structure and sp^2 bonding that has high electrical conductivity within the plane.³⁵ The electrical conductivity of graphene is about 64 mS cm^{-1} which is 60 fold higher than MWCNTs,³⁶ and is an attractive support for nano-catalysts and for electrochemical studies. The two-dimensional nature of graphene allows both the side plates and the skeletal plates to interact with the catalyst. Another significant advantage of graphene, which strongly affects its electrochemical performance, can be attributed to the kinetics of heterogeneous electron transfer, which can be promoted by the presence of oxygen-containing groups on its edge and surface.³⁷

Different nanoparticles on different supports have been used as electrocatalysts for formate oxidation (FO). Ha *et al.* synthesized a $\text{Cu}_x\text{Pd}_{1-x}/\text{C}$ electrocatalyst and used it for FO. Different molar ratios of Cu : Pd have been investigated, and the 20 : 80 ratio showed excellent catalytic activity for formate oxidation compared to the other ratios and the mono-metallic Pd catalyst.³⁸ Manithiram & Yu studied the activity of Pt/C and Pd/C for formate oxidation and concluded that Pd/C has a better performance. Therefore, they used Pd/C and Pt/C as the anodic and cathodic catalysts, respectively. They achieved the highest power density of $75 \text{ mW (mg Pd}^{-1})$ at $60 \text{ }^\circ\text{C}$.³⁹ In the other work, Pd/C was used for formate oxidation in alkaline formate fuel cells.⁴⁰ Huang *et al.* synthesized a CuPdAu/C electrocatalyst with anti-poisoning features and the greatest activity in both acidic and alkaline solutions for formate oxidation.⁴¹ Wang *et al.* investigated the effect of Pd/CNTs and Pd on Ag/CNTs for formate oxidation. The mass-specific chronoamperometric current of the Pd on Ag/CNTs ($171.8 \text{ mA mg Pd}^{-1}$) is two-fold more than that on Pd/CNTs ($70.0 \text{ mA mg Pd}^{-1}$).⁴² Also, Xia *et al.* synthesized Pt-Ag nano-balloons. Under alkaline conditions, electrochemical studies revealed that Pt-Ag nano-balloons had an approximately 19.3 fold activity improvement for the formate oxidation reaction (FOR) compared to commercial Pt nanoparticles.⁴³ In addition to the mentioned studies, other electrocatalysts such as PtAu/C, PdAu/C, AgPd and PdAgRu/CNTs have also been synthesized and used for formate oxidation or in formate fuel cells.⁴⁴⁻⁴⁷

The discussion above highlights several studies of formate oxidation and formate fuel cells in which different nanoparticles were synthesized with alloy structures and supported on vulcan and CNTs. However, to our knowledge there are no reports on equivalent applications of nanoparticles with core-shell structures for formate oxidation and as an anodic catalyst in formate fuel cells, in particular deploying reduced graphene oxide (rGO) as a catalyst support. Therefore, in this research work, M@Pd/N (M = Co, Ni; N = MWCNTs, rGO) were synthesized as anodic catalysts and studied for formate oxidation and in DFHPFC for the first time. For this purpose, first Co@Pd core-shell nanoparticles on MWCNTs were synthesized and studied for formate oxidation and after comparing with Ni@Pd/MWCNT electrocatalysts, in the second step, the effect of rGO as a catalyst support on the performance of Ni@Pd core-shell nanoparticles was investigated for formate oxidation and in a direct formate-hydrogen peroxide fuel cell (DFHPFC). Furthermore, electrochemical impedance spectroscopy EIS studies were undertaken in DFHPFC containing Ni@Pd/rGO (with excellent performance) as the anodic catalyst and Pt/C as the cathodic catalyst. The effect of the discharge current density and temperature on the Nyquist curves was studied.

2. Experimental section

2.1. Synthesis of the Co@Pd/MWCNT electrocatalyst

The Co@Pd/MWCNT electrocatalyst was synthesized using a two-step reduction method as described in our previous work,⁴⁸ with the difference that $\text{CoCl}_2 \cdot 6\text{H}_2\text{O}$ (99.99%, Merck) was used as a precursor for the core formation instead of $\text{NiCl}_2 \cdot \text{H}_2\text{O}$ (99.99%, Merck). Briefly, 96 mg of MWCNT-OH (95%, neutrino Company) was dispersed into a mixture of water: isopropyl alcohol (1 : 3). Then, 5 mL of CoCl_2 solution was added dropwise, and stirred for 1 h to enable dispersion. After adding 60 mg tri-sodium citrate (99%, Merck) as the stabilizing agent, 20 mL of freshly prepared borohydride (96%, Merck) solution containing 40 mg NaOH was added dropwise with vigorous stirring at 75 °C. After 24 h, the synthesized Co/MWCNT electrocatalyst was collected, rinsed well with water and dried at 80 °C. Then, the collected powder was dispersed in ethylene glycol (EG, Merck) for 2 h. After that, 5 mL of HCl 0.04 M containing 28 mg of PdCl_2 (99.99%, Merck) was added and the solution pH was adjusted in the range of 7–8 using NaOH in EG.^{49–51} The mixture was heated for 4 h at 95 °C. Finally, the synthesized Co@Pd/MWCNT electrocatalyst was collected, washed and dried at 80 °C.

2.2. Synthesis of the Ni@Pd/rGO electrocatalyst

Graphene oxide was prepared using the Hummers' method.⁵² The Ni@Pd/rGO electrocatalyst was prepared using a two-step successive reduction method, with reduced graphene oxide as the carbon substrate. First, Ni/rGO was prepared using sodium borohydride as the reducing agent, simultaneously reducing Ni^{2+} to Ni^0 and GO to rGO. For this purpose, 113 mg GO was dispersed in 65 mL distilled water using an ultrasonic bath. After that, 5 mL of NiCl_2 solution (40 mg) was added and stirred for another 1 h. After adding 60 mg tri-sodium citrate, 25 mL of freshly prepared borohydride containing 40 mg NaOH was added dropwise. The solution was refluxed at 100 °C for 3 h. After that, Ni/rGO was collected, washed and dried at 80 °C. In the second stage, the Ni@Pd/rGO electrocatalyst was synthesized according to the approach described in Section 2.1.

2.3. Three electrode investigations

The catalytic performance of the synthesized electrocatalysts in the half-cell configuration was studied using different electrochemical methods such as cyclic voltammetry (CV), chronoamperometry (CA), electrochemical impedance spectroscopy (EIS), and chronopotentiometry (CP). The influence of scan rate, formate concentration and temperature on the voltammograms was evaluated. The required electrocatalyst ink for half-cell studies was obtained by mixing 5 mg of the prepared electrocatalyst powder (Co@Pd/MWCNTs, Ni@Pd/rGO) with 0.1 mL of Nafion solution 5 wt% (Dupont, EC-NS-05), distilled water and isopropyl alcohol and sonicated for 1 h. After that 6 μL of the obtained catalyst ink was placed on the glassy carbon electrode (0.1133 cm^2) as the working electrode. A platinum grid was applied as the counter electrode. Three electrode studies were carried out employing an OrigaFlex made in France (OrigaFlex-OGF01A/Potentiostat/Galvanostat) and the potential was measured with respect to a mercury/mercury oxide (MOE) reference electrode.

2.4. Single fuel cell investigations

The used fuel cell system includes stainless steel end plates, current collectors made of gold-plated stainless steel, and graphite plates with an active surface area of 5 cm² with spiral grooves with a depth of 1 mm. An electronic load device in galvanostat mode was also used to record polarization data. The method is that at each specific current, a resistor is placed in the external circuit of the fuel cell. A voltmeter located at both ends of the cell, and the potential and current can be recorded and $I-V$ and $I-P$ plots constructed. The most critical component of the fuel cell system, which is also the site of electrochemical reactions, is the membrane electrode assembly (MEA). The MEAs were prepared using the catalyst coated membrane (CCM) method. The synthesized core-shell catalysts with a metal loading of 1 mg cm⁻² were used as the anodic catalyst, while Pt/C with a metal loading of 0.5 mg cm⁻² was used as the cathodic catalyst. Catalyst inks were prepared from a mixture of distilled water, isopropyl alcohol and 5 wt% Nafion solution as a binder. After sonication for 1.5 h, this was sprayed onto both sides of the pre-treated Nafion membrane.²⁹ Two carbon cloths containing a gas diffusion layer (GDL) were used as gas diffusion electrodes. The stability curve was recorded by setting the discharging current at 50 mA and recording the fuel cell voltage with respect to time.

2.5. Instrumentations

The morphological investigations and the elemental analysis of the synthesized electrocatalysts were carried out with field emission scanning electron microscopy (FE-SEM, MIRA3FEG-SEM, Tescan), energy dispersive X-ray spectroscopy (EDX) and transmission electron microscopy (TEM, LEO 906 E (100 kV)). HR-TEM was performed using a FEI Tecnai F20 S/TEM electron microscope operating at 200 kV with a field emission gun. The structural investigations of the electrocatalysts were carried out using X-ray diffraction (XRD, Philips-VW 1730) with CuK α radiation. The electronic state of the synthesized electrocatalysts was investigated with X-ray photoelectron spectroscopy (Thermo Scientific, K-alpha Surface Analysis).

3. Results and discussion

3.1. Structural investigations of Co@Pd/MWCNTs

To confirm the synthesis of the Co@Pd nanoparticles on MWCNTs, SEM images of MWCNTs in the absence and presence of Co@Pd nanoparticles are shown in Fig. 1(a) and (b), respectively. The SEM image indicates the tubular structure of the synthesized electrocatalyst in which the nanoparticles were uniformly deposited on the MWCNT surface (Fig. 1(b)). This makes the MWCNT surface rough and rugged. Using MWCNTs increases the porosity and the catalytic active surface area of the synthesized electrocatalysts. Based on the SEM images, the size of the nanoparticles is determined to be about 10 nm. According to the images, after depositing the nanoparticles on the MWCNTs, the thickness of the nanotubes increases compared to the case without nanoparticles.

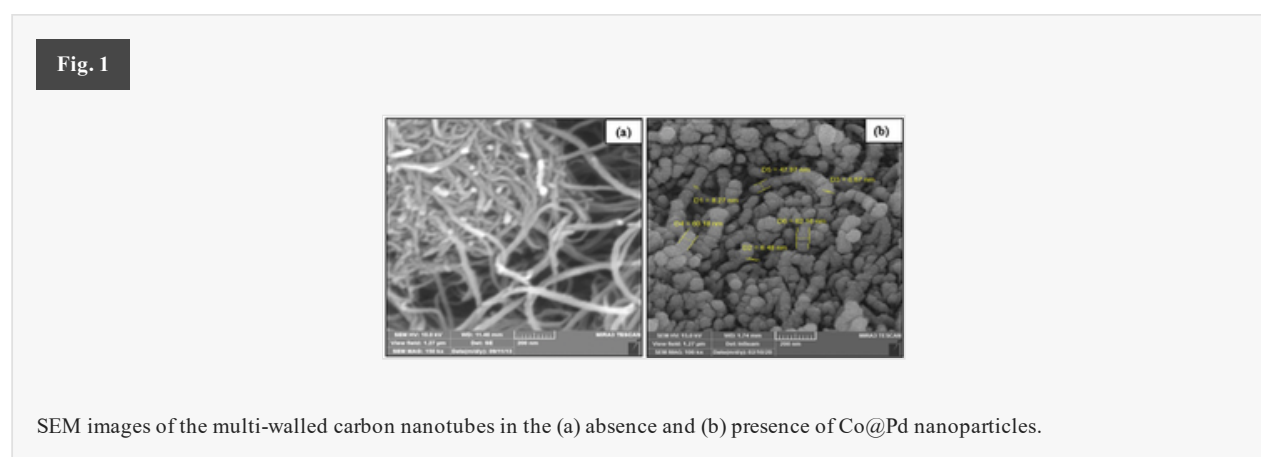


Fig. S1 (ESI[†]) presents the EDX analysis of the Co@Pd/MWCNT electrocatalyst. The presence of Co, Pd and C peaks confirms the successful synthesis of the mentioned electrocatalyst. Based on Fig. S1 (ESI[†]), the mass percentage of metal: MWCNT is about 20 : 80 and the Co to Pd molar ratio is around 1. A TEM image of the Co@Pd/MWCNT electrocatalyst is shown in Fig. S2 (ESI[†]). The tube structure of the multi-walled carbon nanotubes is visible in the image. Also, the black dots are related to Co@Pd nanoparticles that are distributed on the surface of carbon nanotubes, which demonstrates that there is a small accumulation of nanoparticles on the surface of carbon nanotubes.

To investigate the crystal structure of the Co@Pd/MWCNT electrocatalyst, an XRD technique was used, and the results are shown in Fig. S3 (ESI[†]). The peak observed in $2\theta = 25.9^\circ$ is related to the carbon plane (002) of the multi-walled carbon nanotube catalyst substrate. Other diffraction peaks also appear at 2θ equal to 39.6, 45.8, 67.2 and 79.95° , which correspond to the (111), (200), (220) and (311) crystal planes of palladium with a face center cubic (FCC) structure. Apart from the weak peak with $2\theta = 53.5^\circ$, which corresponds to the (200) crystal plane of cobalt,⁵³ no scattering peak of cobalt is observed. This indicates that for these Co@Pd nanoparticles, cobalt has an amorphous structure, or since the particles are very fine particles, they cannot be readily detected using the XRD technique.

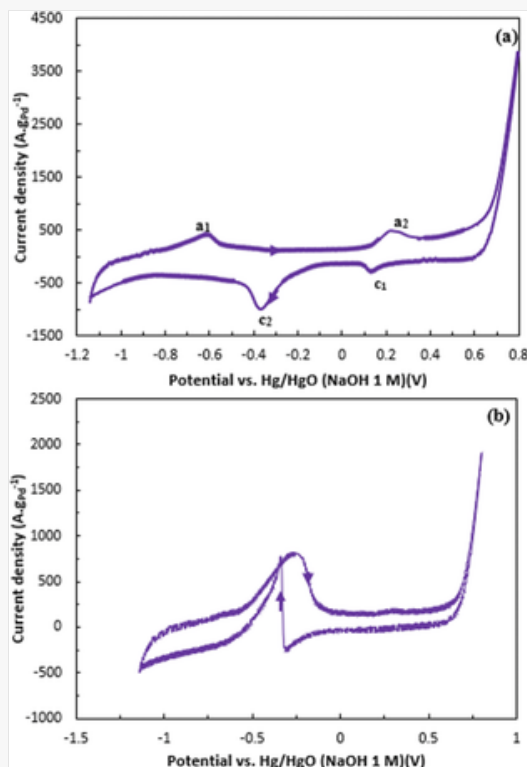
3.2. Half-cell investigations of the Co@Pd/MWCNT electrocatalyst

Cyclic voltammetry curves (CVs) of Co@Pd/MWCNTs in 1 M NaOH in the potential range of -1.1 to 0.8 V (vs. Hg/HgO NaOH 1 M) at a scan rate of 100 mV s^{-1} are shown in Fig. 2(a). Two peaks (a_1 , a_2) appear in the anodic scan and a further two peaks (c_1 , c_2) are apparent in the cathodic scan. The a_1 peak is related to hydrogen desorption,⁵⁴ the a_2 peak corresponds to the formation of Co(OH)_2 or CoO_2 species on the electrode surface,⁵⁵ the c_1 peak relates to the reduction of Co^{2+} to Co^0 ⁵⁶ and peak c_2 is associated with the reduction of palladium oxides that were produced on the electrode surface during anodic scanning.⁴⁸ There are different methods to calculate the electrochemical active surface area (ECSA): (1) by measuring the non-Faradaic capacitive current associated with double-layer charging from the scan-rate dependence of cyclic voltammograms and (2) by measuring the frequency dependent impedance of the system using electrochemical impedance spectroscopy (EIS)⁵⁷ and (3) the BET surface area. Of course, in many reliable articles, the amount of charge required for the reduction of metal oxides formed during anodic scanning has been used to calculate the electrochemical active surface area.^{47,48,58-61} In this study, using eqn (1) and the charge required to reduce palladium oxide the electrochemical active surface area (ECSA) of the electrocatalyst can be estimated. The obtained ECSA value for this catalyst is $310 \text{ m}^2 \text{ g}^{-1}$.

$$\text{ECSA} = \frac{Q_{\text{PdO}}}{0.405 \times [\text{Pd}]}$$

1

Fig. 2



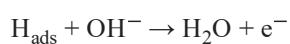
The CVs of Co@Pd/MWCNTs in (a) NaOH 1 M and (b) NaOH 1 M containing HCOONa 0.5 M.

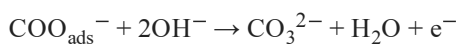
The CVs of the Co@Pd/MWCNTs in 1 M NaOH containing 0.5 M HCOONa within the potential range of -1.1 to 0.8 V (vs. Hg/HgO NaOH 1 M) at the scan rate of 100 mV s^{-1} are presented in Fig. 2(b). In the anodic scan, the peak spanning between -0.6 to -0.07 V (vs. Hg/HgO NaOH 1 M) arises from the formate oxidation on the surface of Co@Pd/MWCNTs. It is considered that the peak during the positive scan corresponds to the direct oxidative pathway of formate to CO_2 (primary pathway) and the peak during the negative scan at about -0.4 V is related to the oxidation of CO which was generated during the dehydration reaction of formate (an indirect pathway of formate oxidation (secondary pathway)).⁶²⁻⁶⁴

The oxidation reaction of formate on the surface of this catalyst is likely to be similar to that characterized on other metal electrodes and can be described as follows: the formate is first adsorbed on the palladium surface and according to the following reaction it dissociates into H_{ads} and $\text{COO}_{\text{ads}}^-$.⁶⁵

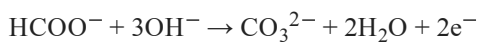


Then H_{ads} and $\text{COO}_{\text{ads}}^-$ can be oxidized by OH^- to form CO_3^{2-} and H_2O :





In general, the half cell reaction of formate on the surface of palladium nanoparticles can be written as follows:



According to Fig. 2(b), the current density related to the formate oxidation on the studied catalyst is approximately equal to $807 \text{ A g}_{\text{Pd}}^{-1}$ and the onset oxidation potential of formate is -0.572 V .

In the following, the effect of sodium formate concentration on CVs in NaOH 1 M was studied and is presented in Fig. S4 (ESI[†]). As expected, when the concentration of sodium formate increases, the oxidation current density also increases on the catalyst surface (Fig. S4(a), ESI[†]) and there is a linear relationship between I_p and C_{Formate} (Fig. S4(b), ESI[†]) according to the Randles–Sevcik equation (eqn (6), although this equation applies strictly to diffusion controlled conditions, while the formate oxidation is likely to be under more complex mixed kinetic control). On the other hand, with increasing sodium formate concentration, the onset potential for formate oxidation shifts slightly to more negative values.

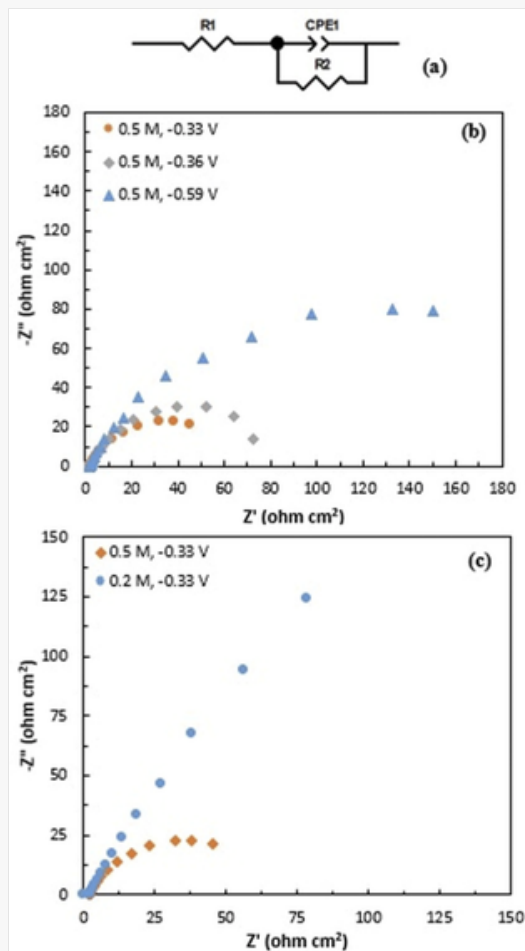
$$I_p = 2.99 \times 10^5 (\alpha n)^{1/2} n A C_0^* D_0^{1/2} \nu^{1/2}$$

Next the influence of different temperatures (298, 308, 318 and 328 K) on the CVs of the Co@Pd/MWCNTs was studied (Fig. S5, ESI[†]). As expected, the current density for the electrooxidation also increases (Fig. S5(a), ESI[†]) as the temperature increases due to the acceleration of the formate oxidation process. In accordance with the Arrhenius equation (eqn (7)), there is a linear relationship between $\ln I_p$ and T^{-1} (Fig. S5(b), ESI[†]).⁶⁶ From the slope of $\ln I_p$ versus T^{-1} , the activation energy for formate oxidation on Co@Pd/MWCNTs was found to be 12.5 kJ mol^{-1} using the equation:

$$E_a = -R \frac{\partial \ln I_p}{\partial (1/T)}$$

To investigate the stability of the Co@Pd/MWCNT electrocatalyst, chronoamperometry and chronopotentiometry curves were recorded in a solution of 1 M NaOH + 0.5 M sodium formate, and these are presented in Fig. S6(a) and (b) (ESI[†]), respectively. The chronoamperometry curve was recorded at a constant potential of -0.37 V . The formate oxidation current density decreases over time until it reaches a steady-state value. A steady-state current density of 169 A g^{-1} was obtained for this catalyst. Also, the chronopotentiometry curve of the Co@Pd/MWCNT catalyst was recorded at a constant current of 0.05 mA . The steady-state potential for formate oxidation on this electrocatalyst was -0.507 V , which is a guide to the required overpotential for formate oxidation.

The impedance technique was used to obtain more information about the electrochemical behavior of the synthesized electrocatalyst. At first, the impedance spectra for the Co@Pd/MWCNT electrocatalyst were obtained in 1 M NaOH solution in the presence of 0.5 M sodium formate for various potentials (-0.59 , -0.36 and -0.33 V). The impedance spectra recorded under these conditions are shown in Fig. 3(b). One semicircle appears in the spectra, which is related to the electro-oxidation of formate on the surface of the Co@Pd/MWCNT catalyst.



(a) The used equivalent circuit for fitting the EIS spectra, the effect of (b) different potentials (-0.59 , -0.36 and -0.33 V) and (c) different formate concentrations (0.2, 0.5 M) on the Nyquist curves of Co@Pd/MWCNTs in 1 M NaOH.

The equivalent circuit applied for fitting of these impedance data is shown in Fig. 3 (a). R_1 is the resistance of solution (R_s), R_2 is the charge transfer resistance (R_{ct}) and C_{PE} is a constant phase element. The semicircle diameter related to the electrochemical reaction of formate oxidation, is smaller at -0.33 V than the other potentials. In other words, through the enhancement in voltage (from -0.59 V to -0.33 V), R_{ct} (the semicircle diameter) was reduced because according to the CV curves at -0.33 V the rate of formate oxidation is the highest in comparison with other potentials. As a result, the lowest charge transfer resistance is obtained at this potential.

The effect of formate concentration on the Nyquist curves of the Co@Pd/MWCNT electrocatalyst (Fig. 3(c)) has also been examined. Increasing the formate concentration from 0.2 to 0.5 M at a constant potential (-0.33 V), led to the charge transfer resistance values decreasing. This can be explained by an increase of the formate concentration leading to an increase in the concentration of the electroactive species at the surface, which consequently increases the rate of the charge transfer process and reduces the associated resistance. The recorded impedance curves have been fitted with the equivalent circuit in Fig. 3(a) and the obtained charge transfer resistance values under different potentials and concentrations are summarized in Table 1.

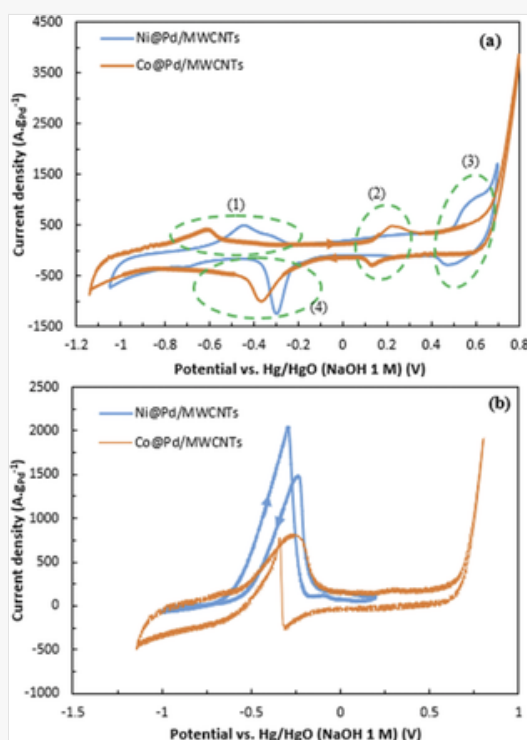
Table 1

R_{ct} values obtained for Co@Pd/MWCNTs at different formate concentrations (0.5, 0.2 M) and different potentials (-0.59 , -0.36 and -0.33 V)

Electrocatalyst	Concentration (M)	Voltage (V)	R_{ct} (Ohm cm^2)
Co@Pd/MWCNTs	0.5	-0.59	225
		-0.36	79
		-0.33	55
	0.2	-0.33	650

After studying the performance of the Co@Pd/MWCNT catalyst for formate oxidation using electrochemical techniques in a half-cell configuration, the obtained cyclic voltammetry curves of Co@Pd/MWCNTs in 1 M NaOH in the absence and the presence of formate were compared with the CVs of the Ni@Pd/MWCNT catalyst. This comparison is shown in Fig. 4. The CVs of the two core-shell electrocatalysts (Co@Pd/MWCNTs and Ni@Pd/MWCNTs) with the same catalyst support (MWCNTs) in 1 M NaOH at a scan rate of 100 mV s⁻¹ are presented in Fig. 4(a). As previously described, the peaks in region 1 arise from hydrogen desorption from the catalyst surface.^{67,68} Also, the observed peaks in regions 2 and 3 are related to the reversible reaction of Co²⁺/Co (Co@Pd/MWCNTs)^{55,56} and Ni²⁺/Ni³⁺ (Ni@Pd/MWCNTs)⁶⁹ in alkaline media, respectively.

Fig. 4



The CVs of Ni@Pd/MWCNTs and Co@Pd/MWCNTs in (a) 1 M NaOH and (b) 1 M NaOH containing 0.5 M HCOONa.

The peak in region 4 corresponds to the reduction of produced PdO during the anodic scan on the related catalyst's surface.⁴⁸ The ECSA value for each electrocatalyst was calculated from the required charge for reduction of the produced PdO. Using eqn (1), the ECSA values were 313 and 310 m² g⁻¹ for Ni@Pd/MWCNTs and Co@Pd/MWCNTs, respectively.

For comparison, the CVs of Ni@Pd/MWCNTs and Co@Pd/MWCNTs in NaOH 1 M containing sodium formate 0.5 M are presented in Fig. 4(b). The current density and onset potential of formate oxidation reaction on the studied electrocatalysts are summarized in Table 2.

Table 2

The current density and onset potential of formate oxidation on Ni@Pd/MWCNTs and Co@Pd/MWCNTs electrocatalysts

Electrocatalyst	Onset potential (V)	Current density (A.g ⁻¹)
Ni@Pd/MWCNTs		
Co@Pd/MWCNTs		

Electrocatalysts	Current density of formate oxidation ($A g^{-1}$)	Onset potential of formate oxidation (V)
Ni@Pd/MWCNT	1443	-0.635
Co@Pd/MWCNT	807	-0.572

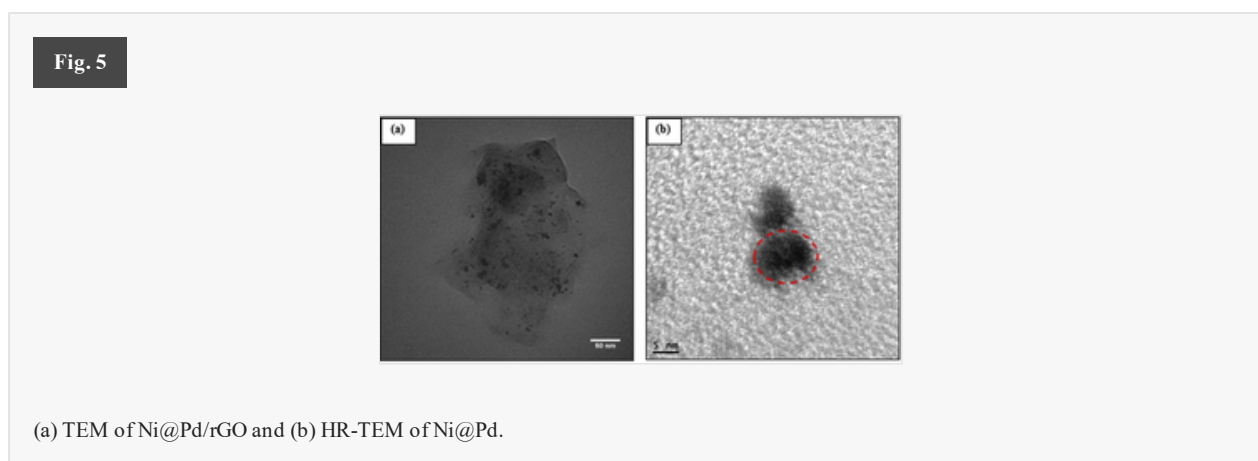
According to the ECSA, the current density and onset potential of formate oxidation values on the studied electrocatalysts, it can be concluded that the presence of Ni in the core instead of the Co increases the catalytic performance of the catalyst due to the synergistic effects between Ni and Pd.^{58,70,71} Therefore, in the next stage of the present research work involving investigation of the effect of catalyst support on the catalyst performance toward formate oxidation, we decided to synthesize and study Ni@Pd nanoparticles (with higher catalytic behavior compared to the Co@Pd) on reduced graphene oxide (rGO). Hence, the following section describes the use of reduced graphene oxide as the catalyst support instead of multi-walled carbon nanotubes.

It is expected that the Ni@Pd/rGO catalyst has better catalytic activity than Ni@Pd/MWCNTs for formate oxidation because the reduced graphene oxide nanosheets have a larger active surface area than carbon nanotubes.

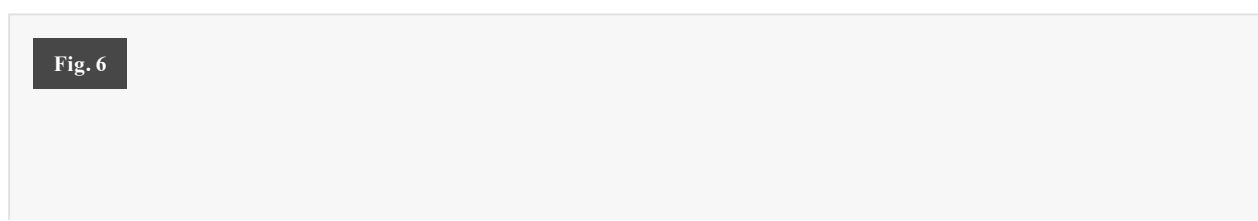
3.3. Structural investigations of Ni@Pd/rGO

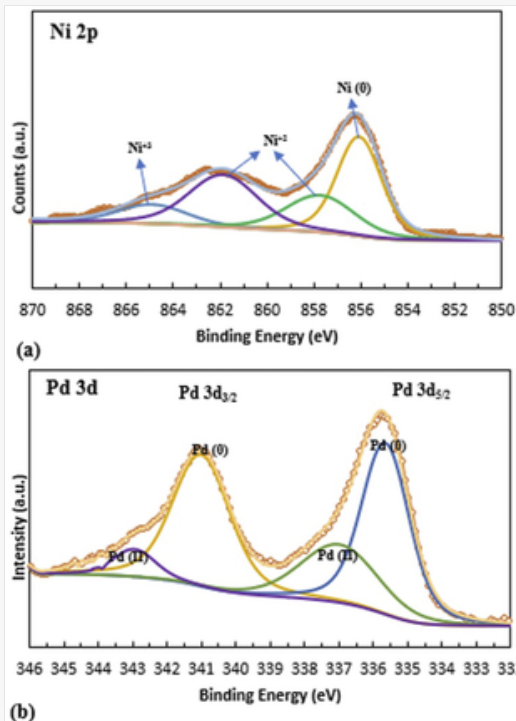
The SEM images of reduced graphene oxide plates without any nanoparticles and reduced graphene oxide containing Ni@Pd core-shell nanoparticles were presented in our previous work.⁷² In SEM images, the planar structure of reduced graphene oxide is visible. After deposition of nanoparticles, the surface of the reduced graphene oxide plates becomes rough, which increases the active surface area of the synthesized catalyst. Also, according to the SEM images, the nanoparticles are uniformly deposited on the surface of the reduced graphene oxide plates, and the approximate size of nanoparticles was computed to be around 10–13 nm.⁷² Also, the weight percentage of metal to carbon is about 20 to 80 and the weight proportion of Ni to Pd is approximately 1 : 1.⁷²

From the TEM image of Ni@Pd/rGO and the HR-TEM of Ni@Pd nanoparticles presented in Fig. 5, the layered structure of graphene oxide can be clearly seen with nanoparticles uniformly distributed on its surface. The contrasting difference observed between the core and the shell confirms that the synthesized nanoparticles have a core-shell structure. According to the HR-TM, the approximate size of the nanoparticles was found to be around 10 nanometers.



In the XPS spectrum of Ni 2p_{3/2} presented in Fig. 6a, the peaks of Ni⁰, Ni⁺² and Ni⁺³ can be seen. The peak at the binding energy of 856 eV corresponds to metallic nickel (Ni⁰) with a content of 40%, the peaks at the binding energies of 857.70 and 861.80 eV are related to Ni⁺² (NiO 19% and Ni(OH)₂ 30%) and the peak at 864.83 eV is related to Ni⁺³ (NiOOH 11%).^{73–76} The majority of the nickel is in the form of nickel hydroxide because nickel can be oxidized in the later stages of the synthesis. The presence of these nickel hydroxides improves the electron and proton conductivity of the catalyst.⁷⁷





The XPS spectra of (a) Ni 2p_{3/2} and (b) Pd 3d in Ni@Pd/rGO.

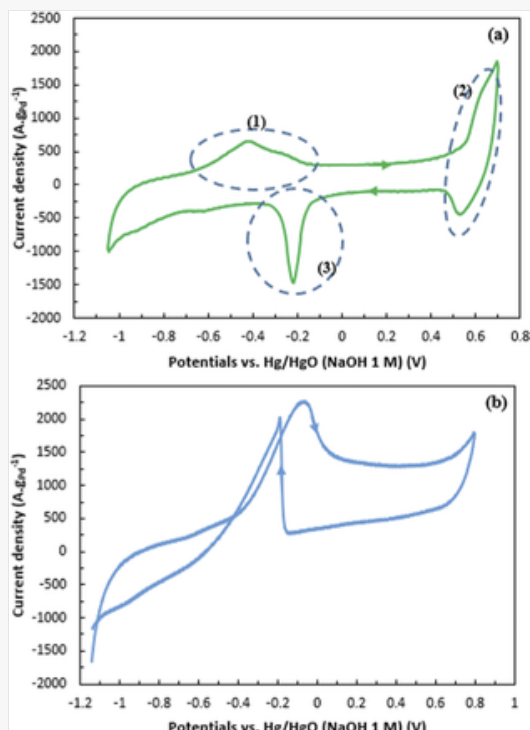
Two doublet peaks are also observed in the XPS spectrum of Pd 3d, with the main constituent being Pd⁰.

The peaks of Pd⁰ (81%) are observed at binding energies of 335.66 and 341.01 eV and the peaks of PdO (19%) are observed at binding energies of 336.99 and 342.95 eV.⁷²

3.4. Half-cell investigations of the Ni@Pd/rGO electrocatalyst

The CVs of Ni@Pd/rGO in 1 M NaOH in the potential range from -1.1 to 0.7 V (Hg/HgO NaOH 1 M) at the scan rate of 100 mV s⁻¹ are shown in Fig. 7(a). As previously described, the peaks in region (1) are associated to hydrogen desorption and the formation of surface Pd oxide on the catalyst surface.⁷² The peak marked in region (2) is due to the electrochemical redox conversion between Ni²⁺/Ni³⁺ during anodic and cathodic sweeping. Another peak also appears during the cathodic scan in region (3), which is related to the reduction of palladium oxides created during the anodic scan on the catalyst surface. From the charge required to reduce palladium oxide, and by using eqn (1), the ECSA value for the Ni@Pd/rGO catalyst was calculated to be 342 m² g⁻¹. The obtained ECSA value for the Ni@Pd/rGO catalyst is about 1.11 and 1.09 times higher than the obtained ECSA values for the Co@Pd/MWCNT (310 m² g⁻¹) and Ni@Pd/MWCNT (313 m² g⁻¹) catalysts, respectively. This shows that the catalyst support influences the catalytic activity of the catalyst with the same nanoparticle type.

Fig. 7



The CVs of Ni@Pd/rGO in (a) 1 M NaOH and (b) 1 M NaOH + 0.5 M HCOONa.

A CV of the Ni@Pd/rGO electrocatalyst in a solution of 1 M NaOH + 0.5 M sodium formate is shown in Fig. 7(b). The current density and the onset potential of formate oxidation are 2260 A g^{-1} and -0.437 V , respectively. It was observed that Ni@Pd/rGO has excellent activity for formate oxidation and is superior to Ni@Pd/MWCNTs and Co@Pd/MWCNTs. The oxidation current density of formate on the Ni@Pd/rGO catalyst is 1.57 and 2.80 times higher than the oxidation current density of formate on Ni@Pd/MWCNT and Co@Pd/MWCNT catalysts, respectively.

Next, the effect of concentration on CVs was investigated, and the results are shown in Fig. S7 (ESI[†]). As fully explained earlier, the current density also increases with increasing concentration according to the Randles–Sevcik equation (eqn (6)) (Fig. S7(a), ESI[†]) and there is a linear relationship between the concentration and the formate oxidation current density (Fig. S7(b), ESI[†]).

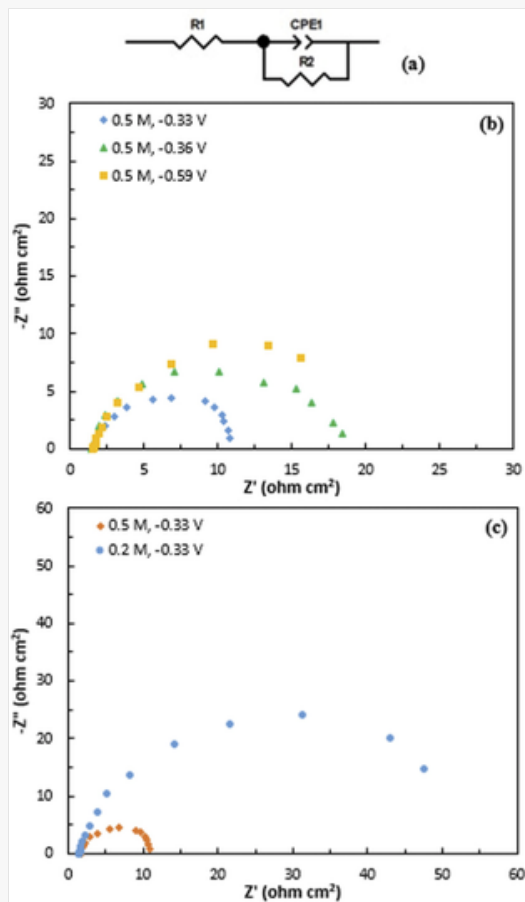
The effect of different temperatures on the CVs of the Ni@Pd/rGO catalyst in an alkaline solution containing 0.5 M sodium formate was investigated, and the results are shown in Fig. S8 (ESI[†]). According to the Arrhenius equation (eqn (7)), as the temperature increases, the current density also increases (Fig. S8(a), ESI[†]), and there is a linear relationship between $\ln I_p$ and T^{-1} (Fig. S8(b), ESI[†]). From the slope of the line obtained for the $\ln I_p$ versus T^{-1} , an activation energy of $11.33 \text{ kJ mol}^{-1}$ was obtained, which is less than the activation energy required for formate oxidation on the surface of Co@Pd/MWCNTs ($12.53 \text{ kJ mol}^{-1}$). A lower activation energy indicates the better catalytic performance of the catalyst, so as for the previous results, the Ni@Pd/rGO catalyst shows more catalytic activity than Co@Pd/MWCNTs.

The chronoamperometry curve for the Ni@Pd/rGO catalyst in alkaline solution containing 0.5 M HCOONa at -0.37 V for 750 s is shown in Fig. S9(a) (ESI[†]). This potential is chosen since it is approximately the onset potential of formate oxidation. According to Fig. S9(a) (ESI[†]), the current density decreases over time until it reaches a steady-state. The steady-state current density for this catalyst was 840 A g^{-1} . Compared to the chronoamperometry curve recorded for the Co@Pd/MWCNT catalyst (Fig. S6(a), ESI[†]), the steady-state current density for the Ni@Pd/rGO catalyst is higher than that for the Co@Pd/MWCNT catalyst.

The chronopotentiometry curve for the Ni@Pd/rGO electrocatalyst is also shown in Fig. S9(b) (ESI[†]). The steady-state potential for formate oxidation on the catalyst is -0.537 V. The steady-state potential for formate oxidation on the Ni@Pd/rGO catalyst is lower than the steady-state potential on the Co@Pd/MWCNT catalyst. This phenomenon indicates that the required potential for formate oxidation on the Ni@Pd/rGO catalyst is less than the required potential for formate oxidation on the Co@Pd/MWCNT catalyst. Therefore, formate is more easily oxidized on the Ni@Pd/rGO catalyst than on the Co@Pd/MWCNTs catalyst.

To further study the catalytic behavior of Ni@Pd/rGO, its impedance spectra were taken in 0.5 M HCOONa + 1 M NaOH solution at different potentials (-0.59 , -0.36 and -0.33 V), as shown in Fig. 8(b). A semicircle was observed that is due to the electrochemical reaction. The corresponding equivalent circuit is shown in Fig. 8(a) where R_s is the electrolyte resistance, and R_{ct} is the charge transfer resistance. After fitting the impedance curves with the corresponding equivalent circuit, the values of R_{ct} can be determined. The values of R_{ct} in different potentials are listed in Table 3. According to this table, at a constant concentration of sodium formate (0.5 M), the value of R_{ct} decreases with increasing potential from -0.59 V to -0.33 V. This agrees well with the cyclic voltammetry curves since at the potential of -0.59 V, the faradaic process takes place on the electrode surface slower than -0.33 V. So, at the potential of -0.59 V, the charge transfer resistance has the highest value. With increasing potential the charge transfer resistance decreases. The lowest value of charge transfer resistance is obtained at the potential of -0.33 V (the potential at which the faradaic process of formate oxidation begins). Also, when the sodium formate concentration was decreased from 0.5 M to 0.2 M at a constant potential of -0.33 V the value of R_{ct} increased (Fig. 8(c)). The decreasing concentration of the electroactive species clearly decreases the rate of the charge transfer process, and increases the corresponding resistance. The obtained R_{ct} values for the catalyst are summarized in Table 3.

Fig. 8



(a) The used equivalent circuit, the effect of different (b) potentials (-0.59 , -0.36 and -0.33 V) and (c) formate concentrations (0.2 and 0.5 M) on Nyquist curves of Ni@Pd/rGO in NaOH 1 M.

Table 3

The R_{ct} values for Ni@Pd/rGO at different formate concentrations (0.2, 0.5 M) and different potentials (-0.59 , -0.36 and -0.33 V)

Electrocatalyst	Concentration (M)	Potential (V)	R_{ct} (Ohm cm^2)
Ni@Pd/rGO	0.5	-0.59	27
		-0.36	16.0
		-0.33	9.9
	0.2	-0.33	52.9

By comparing Tables 1 and 3, it can be stated that the Ni@Pd/rGO catalyst shows the lowest charge transfer resistance (the highest electron conductivity) and, as a result, has better catalytic performance for formate oxidation compared to the Co@Pd/MWCNT catalyst. This is in good agreement with results obtained from other electrochemical techniques such as CA, CP and CV.

3.5. The single formate-hydrogen peroxide fuel cell investigations of Ni@Pd/MWCNT, Co@Pd/MWCNT and Ni@Pd/rGO electrocatalysts

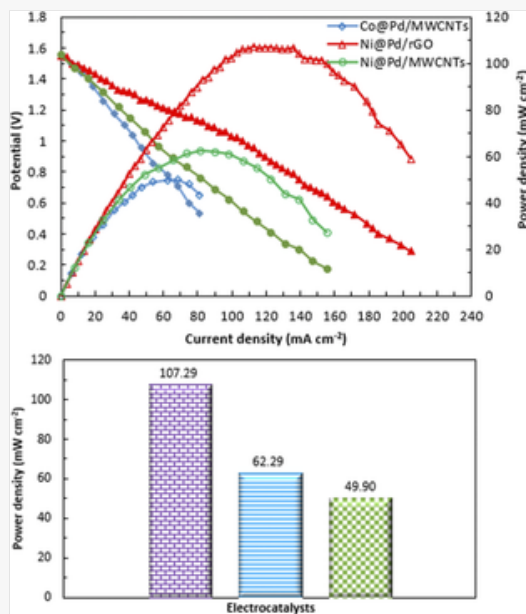
The influence of various anodic electrocatalysts (Ni@Pd/MWCNT, Co@Pd/MWCNT and Ni@Pd/rGO) with a metal loading of 1 mg cm^{-2} in the presence of the same cathodic catalyst (Pt/C with a metal loading of 0.5 mg cm^{-2}) was evaluated in terms of the performance of single formate fuel cells. Formate and hydrogen peroxide were used as the fuel and oxidant, respectively. At first, the fuel, oxidant concentration and temperature were optimized for MEAs prepared with Co@Pd/MWCNT and Ni@Pd/rGO anodic catalysts. For this purpose, alkaline NaOH solution (2 M) containing different concentrations of formate (0.5, 1 and 2 M) as the anolyte and acidic H_2SO_4 solution (0.5 M) containing a constant concentration of H_2O_2 (0.5 M) as the catholyte were flowed over the anode and the cathode sides of the fuel cell, respectively. Then, the $I-V$ and $I-P$ curves were plotted for each of the formate concentrations and the optimum formate concentration at which the maximum power density was obtained. Then, at the optimum concentration of formate (1 M), the $I-V$ and $I-P$ curves were plotted for various concentrations of hydrogen peroxide (0.5, 1, 2 and 3 M). The optimum concentration for hydrogen peroxide was obtained at which the power density is maximum. Finally, at optimal concentrations of formate (1 M) and hydrogen peroxide (2 M), the influence of temperature on the $I-V$ and $I-P$ curves was studied.

The $I-V$ and $I-P$ curves for the Co@Pd/MWCNT anodic catalyst at different concentrations of formate, hydrogen peroxide and different temperatures are shown in Fig. S10(a)–(c) (ESI[†]), respectively. According to Fig. S10(a) (ESI[†]), it is shown that by increasing the concentration of sodium formate from 0.5 M to 1 M at a constant concentration of hydrogen peroxide (0.5 M), the power density increases from 20.1 mW cm^{-2} to 22.3 mW cm^{-2} . This is due to the improvement of the mass transfer process of sodium formate and acceleration of its oxidation. However, at higher concentrations (2 M), the power density decreases from 22.3 mW cm^{-2} (1 M) to 20.8 mW cm^{-2} (2 M). This is presumably due to an increase of sodium formate crossover through the membrane. Therefore, the concentration of 1 M was chosen as the optimal concentration for sodium formate. After that, for optimizing the concentration of hydrogen peroxide with the optimal concentration of sodium formate (1 M), different concentrations of hydrogen peroxide were used as the catholyte of the fuel cell. As shown in Fig. S10(b) (ESI[†]), by increasing the concentration of hydrogen peroxide from 0.5 M to 2 M, the power density increases from 22.3 mW cm^{-2} to 36.7 mW cm^{-2} due to the improvement of the mass transfer of hydrogen peroxide. But, at concentrations higher than 2 M (namely at 3 M), the power density decreases from 36.7 mW cm^{-2} to 29.3 mW cm^{-2} . This is presumably due to increasing the hydrogen peroxide crossover through the membrane, leading to an increase in the decomposition rate and consequent production of gas bubbles at the catalyst surface, thereby decreasing the active surface area of the electrode. Therefore, the concentration of 2 M was chosen as the optimal concentration for hydrogen peroxide.

Finally, at the optimal concentrations of sodium formate (1 M) and hydrogen peroxide (2 M), the influence of temperature on the $I-V$ and $I-P$ curves was investigated (Fig. S10(c), ESI[†]). As shown, with increasing the temperature from $25 \text{ }^\circ\text{C}$ to $60 \text{ }^\circ\text{C}$, the power density increases from 36.7 mW cm^{-2} to 49.9 mW cm^{-2} due to an improvement of the mass transfer of the reactants, increasing the kinetics of the sodium formate oxidation, and the H_2O_2 reduction reactions. The anolyte and catholyte viscosity would also be expected to decrease leading to a conductivity increase. The effect of fuel and oxidant concentration and temperature on the $I-V$ and $I-P$ curves of the Ni@Pd/rGO catalyst was also studied, as shown in Fig. S11 (ESI[†]).

After obtaining optimal concentrations for fuel (1 M) and oxidant (2 M), the influence of various anodic electrocatalysts (Ni@Pd/MWCNT, Co@Pd/MWCNT and Ni@Pd/rGO) on the performance of formate fuel cells were compared at $60 \text{ }^\circ\text{C}$, as shown in Fig. 9.

Fig. 9



(a) The recorded $I-V$ and $I-P$ curves and (b) a columnar graph showing the power density of various anodic electrocatalysts (Co@Pd/MWCNT, Ni@Pd/MWCNT and Ni@Pd/rGO) in the formate fuel cell using 2 M NaOH + 1 M HCOONa as the anolyte and 0.5 M H₂SO₄ + 2 M H₂O₂ as the catholyte.

These figures show the effect of the core material type and the catalyst substrate on the performance of the formate fuel cell. Similar to the results obtained for the three-electrode tests, these single fuel cell tests also show that the presence of nickel in the core increases the performance of single fuel cells and as a result increases their output power density. This is due to the synergistic effects between nickel and palladium, as compared to that between palladium and cobalt. Furthermore, the use of rGO as the catalyst support instead of MWCNTs improves the performance of the formate fuel cell and increases its output power. This is because, as described earlier, rGO has a higher surface area and porosity than MWCNTs. As a result, it increases the electrochemically active surface area of the synthesized electrocatalyst. Also, the impedance spectra (Tables 1 and 3) confirm the highest electron conductivity of the graphene-based electrocatalysts compared to the MWCNT-based ones. Therefore, graphene-based electrocatalysts increase fuel cell efficiency, performance and output power density. The power density obtained for different electrocatalysts under various conditions in direct formate fuel cells are summarized in Table 4.

Table 4

Comparing the performance of different electrocatalysts in DFFCs

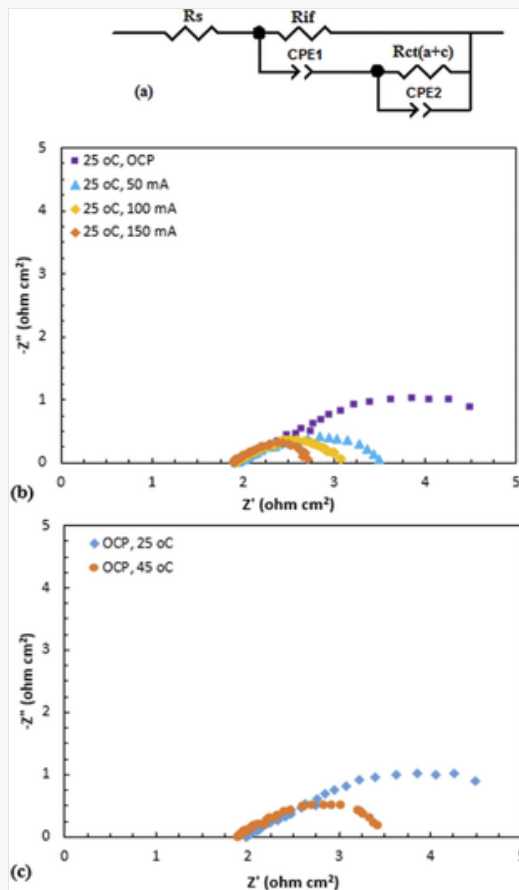
Anode catalyst	Cathode catalyst	Membrane	T (°C)	Power density (mW cm ⁻²)	Ref
PdAu/C 50 : 50 (2 mg cm ⁻²)	Pt/C (2 mg cm ⁻²)	Nafion 117	60	12.3	78
Pd/C (2 mg cm ⁻²)	Pt/C (2 mg cm ⁻²)	Nafion 117	60	12.6	78
Pd/C (2 mg cm ⁻²)	Pt/C (2 mg cm ⁻²)	Tokuyama A201	60	125	79
F-shaped Pd@CC electrode	F-shaped Pd@CC electrode	Na ₂ SO ₄ -soaked PAM gel	25	8.9	80
PdAu/C 50 : 50 (2 mg cm ⁻²)	Pt/C (2 mg cm ⁻²)	Nafion 117	60	12.3	81
PdAu/Ni foam (3 mg cm ⁻²)	PdAu/Ni foam (3 mg cm ⁻²)	Nafion 115	25	214	82
Co ₁ Pd ₁ -MWCNTs (1 mg cm ⁻²)	Pt/C (0.5 mg cm ⁻²)	Nafion 117	60	49.9	This work
Ni ₁ Pd ₁ -MWCNTs (1 mg cm ⁻²)	Pt/C (0.5 mg cm ⁻²)	Nafion 117	60	62.3	This work
Ni ₁ Pd ₁ -rGO (1 mg cm ⁻²)	Pt/C (0.5 mg cm ⁻²)	Nafion 117	60	107.3	This work

Next the single formate-hydrogen peroxide fuel cell with the best performance for formate electrooxidation with the Ni@Pd/rGO catalyst was studied using an electrochemical impedance technique. Impedance tests were performed at optimal concentrations of anolyte (2 M NaOH + 1 M HCOONa) and catholyte (0.5 M H₂SO₄ + 2 M H₂O₂). The effect of the discharge current density (Fig. 10(b)) and temperature (Fig. 10(c)) on Nyquist diagrams was investigated. The Nyquist diagrams show two compressed and overlapping semicircles over the studied frequency range. These Nyquist plots can be divided into 2 regions, the first semicircle at higher frequencies and the second semicircle at lower frequencies. The first semicircle is associated with the interface between the membrane and the electrodes and is called a capacitive or non-faradaic loop, since no charge transfer reactions takes place here.⁸³ As a result, this loop does not change much with changes in the discharge current density and the operating temperature of the fuel cell. The second semicircle is called the faradaic loop, since it is associated with faradaic reactions at the anode and cathode surfaces and is thus affected by the discharge current density and the temperature of the fuel cell. The equivalent circuit used to fit the Nyquist plots is shown in Fig. 10(a). R_s refers to the electrolyte resistance. The electrolyte in the DFHPFC is the Nafion membrane, and its resistance value can be obtained from the intersection of the first semicircle with the x -axis in the high-frequency region. Therefore, the change in R_s values at various discharging currents (0, 50, 100 and 150 mA) and temperatures (25 °C and 45 °C) is low. CPE_1 is an interface capacitance and R_{if} is the interface resistance between the electrodes and the membrane, which can be determined from the capacitive loop. CPE_2 and $R_{ct(a+c)}$ are related to faradaic capacitance and charge transfer resistance. These arise from both anodic and cathodic reactions on the surface of the anodic and cathodic catalyst layers and they can be determined from the faradaic loop and thus $R_{ct(a+c)}$ is decreased with an enhancement in the overpotential. The values for these elements can be obtained by fitting Nyquist plots with the equivalent circuit shown in Fig. 10(a) and the parameters are summarized in Table 5. A comparison of the $R_{ct(a+c)}$ values at different discharging currents (0, 50, 100 and 150 mA) indicates that $R_{ct(a+c)}$ decreases with enhancement in the discharging current (according to eqn (8)):

$$R_{ct} = \frac{dE}{dI} \rightarrow I = \text{constant}(R_{ct})^{-1}$$

8

Fig. 10



(a) Equivalent circuit used to fit the impedance spectra. The effect of (b) discharging current density and (c) the fuel cell operating temperature on Nyquist curves.

Table 5

The obtained impedance parameters for DFHPFC with Ni@Pd/rGO anodic and Pt/C cathodic electrocatalysts under different discharging current densities and temperatures

T (°C)	Discharging current density (mA)	R_s (Ohm cm^2)	$R_{ct(a+c)}$ (Ohm cm^2)
25	0	1.90	3.42
	50	1.89	1.57
	100	1.90	1.04
	150	1.88	0.84
45	0	1.89	1.48

Also, the $R_{ct(a+c)}$ values were decreased when increasing the temperature from 25 °C to 45 °C. This is because the increase in temperature accelerates the rate of electrochemical reactions and as a result increases the current density and according to eqn (8) leads to a decrease in $R_{ct(a+c)}$.

According to Table 5, the R_s values are almost constant and do not change significantly with either changes in discharge current density and fuel cell temperature. However, as shown, the charge transfer resistance decreases with increasing discharge current density and fuel cell temperature.

Conclusions

In this study, the effects of core materials ($M = \text{Ni}, \text{Co}$) and catalyst supports ($N = \text{MWCNTs}, \text{rGO}$) on the performance of the $M@Pd/N$ electrocatalysts were evaluated. The obtained results showed that the presence of Ni at the core instead of Co improved the catalytic performance of the electrocatalyst due to the synergistic effects between Ni and Pd. In

other words, the formate oxidation current density on Ni@Pd/MWCNTs is 1.78 times higher than that on Co@Pd/MWCNTs. Also, using rGO as the catalyst support increases the catalytic activity of the catalysts in comparison with MWCNTs because of its higher surface area and electron conductivity. As the results show, the formate oxidation current density and ECSA values on Ni@Pd/rGO are 1.57 and 1.09 times higher than those on Ni@Pd/MWCNTs, respectively. Also, from single DFHPFC studies, the maximum power densities of 49.9, 62.3 and 107.3 mW cm⁻² were obtained for Co@Pd/MWCNTs, Ni@Pd/MWCNTs and Ni@Pd/rGO, respectively. Therefore, in single fuel cell studies, the influence of the core material and catalyst support on the performance of the fuel cell can be seen.


Conflicts of interest

There are no conflicts to declare.

Acknowledgements

We sincerely thank the Nanotechnology Initiative Council of Iran. We also acknowledge the Iran National Science Foundation (INSF) for the support under grant number 97018389 and the International Academic Cooperation Directorate in University of Tabriz under grant number TabrizU300-14 program.

Notes and references

 References can be edited in the panel that appears to the right when you click on a reference.

- 1 R. Russell, *The Greenhouse Effect & Greenhouse Gases*, University Corporation for Atmospheric Research Windows to the Universe, 2007
- 2 A. A. C. Staudt, N. Huddleston and S. Rudenstein, *Bull. Am. Meteorol. Soc.*, *Natl. Acad. Sci.* **2008**, **200789**, 14975–985.
- 3 B. Mundial, *World Development Report 2010: Development and Climate Change*, 2010
- 4 N. Rajalakshmi, N. Lakshmi and K. S. Dhathathreyan, *Int. J. Hydrogen Energy*, 2008, **33**, 7521–7526.
- 5 E. Ticianelli, C. Derouin, A. Redondo and S. Srinivasan, *J. Electrochem. Soc.*, 1988, **135**, 2209–2214.
- 6 F. Barbir, *PEM fuel cells: theory and practice*, Elsevier Academic Press, 2005
- 7 N. Sammes, *Fuel cell technology: reaching towards commercialization*, Springer, 2006
- 8 R. Ojani, R. Valiollahi and J. B. Raoof, *Appl. Surf. Sci.*, 2014, **311**, 245–251.
- 9 H. Nagar, N. Sahu, V. V. B. Rao and S. Sridhar, *Renewable Energy*, 2020, **146**, 1262–1277.
- 10 V. Johánek, A. Ostroverkh and R. Fiala, *Renewable Energy*, 2019, **138**, 409–415.
- 11 C. Simari, C. L. Vecchio, V. Baglio and I. Nicotera, *Renewable Energy*, 2020, **159**, 336–345.
- 12 M. G. Hosseini, R. Mahmoodi and M. Abdolmaleki, *New J. Chem.*, 2018, **42**, 12222–12223.
- 13 T. H. Oh, *Renewable Energy*, 2021, **178**, 1156–1164.
- 14 A. Uzundurukan, E. S. Akça, Y. Budak and Y. Devrim, *Renewable Energy*, 2021, **172**, 1351–1364.

- 15 T. H. Oh, *Renewable Energy*, 2021, **163**, 930–938.
- 16 L. Lan, J. Li, Y. Yang, L. Zhang, L. Zhang, Q. Fu, X. Zhu and Q. Liao, *Carbon*, 2021, **189**, 240–250.
- 17 X. Cheng, R. Chen, X. Zhu, Q. Liao, X. He, S. Li and L. Li, *Int. J. Hydrogen Energy*, 2016, **41**, 2457–2465.
- 18 L. An, T. S. Zhao, Z. H. Chai, P. Tan and L. Zeng, *Int. J. Hydrogen Energy*, 2014, **39**, 19869–19876.
- 19 Y. S. Li, Y. L. He and W. W. Yang, *J. Power Sources*, 2015, **278**, 569–573.
- 20 X. W. Yu and A. Manthiram, *Appl. Catal., B*, 2015, **165**, 63–67.
- 21 L. An, T. S. Zhao, S. Y. Shen, Q. X. Wu and R. Chen, *Int. J. Hydrogen Energy*, 2010, **35**, 4329–4335.
- 22 E. Kjeang, R. Michel, D. A. Harrington, D. Sinton and N. Djilali, *Electrochim. Acta*, 2008, **54**, 698–705.
- 23 H. Kuroki, S. Miyanishi, A. Sakakibara, Y. Oshiba and T. Yamaguchi, *J. Power Sources*, 2019, **438**, 226997.
- 24 Y. S. Li, H. Wu, Y. L. He, Y. Liu and L. Jin, *J. Power Sources*, 2015, **287**, 75–80.
- 25 J. Noborikawa, J. Lau, J. Ta, S. Hu, L. Scudiero, S. Derakhsha and S. Ha, *Electrochim. Acta*, 2014, **137**, 654–660.
- 26 X. W. Yu and A. Manthiram, *Appl. Catal., B*, 2015, **165**, 63–67.
- 27 D. Sun, L. Si, G. Fu, C. Liu, D. Sun and Y. Chen, *J. Power Sources*, 2015, **280**, 141–146.
- 28 M. S. Ureta-Zar~nartu, C. Mascayano and C. Gutierrez, *Electrochim. Acta*, 2015, **165**, 232–238.
- 29 M. G. Hosseini and R. Mahmoodi, *Int. J. Hydrogen Energy*, 2017, **42**, 10363–10375.
- 30 J.-J. Wang, Y.-T. Liu, I.-L. Chen, Y.-W. Yang, T.-K. Yeh, C. H. Lee, C.-C. Hu, T.-C. Wen, T.-Y. Chen and T.-L. Lin, *J. Phys. Chem. C*, 2014, **118**, 2253–2262.
- 31 S. Ali, R. Ahmed, M. Sohail, S. A. Khan and M. S. Ansari, *J. Ind. Eng. Chem.*, 2015, **28**, 344–350.
- 32 Y. Zhao, X. Yang, J. Tian, F. Wang and L. Zhan, *Int. J. Hydrogen Energy*, 2010, **35**, 3249–3257.
- 33 Z.-q Yang, P.-c Zhao and Z.-l Xie, *Carbon*, 2012, **50**, 2061–2064.
- 34 A. L. Dicks, *J. Power Sources*, 2006, **156**, 2, 128–141.
- 35 W. Yang, K. R. Ratinac, S. P. Ringer, P. Thordarson, J. J. Gooding and F. Braet, *Angew. Chem., Int. Ed.*, 2010, **49**, 2114–2138.
- 36 M. Pumera, *Chem. Rec.*, 2009, **9**, 211.
- 37 D. A. C. Brownson and C. E. Banks, *Analyst*, 2010, **135**, 2768–2778.
- 38 W. J. Wang, S. Hwang, T. Kim, S. Ha and L. Scudiero, *Electrochim. Acta*, 2021, **387**, 138531.
- 39 X. Yu and A. Manthiram, *Appl. Catal., B*, 2015, **165**, 63–67.

- 40 M. Choun and J. Lee, *J. Energy Chem.*, 2016, **25**, 683–690.
- 41 H. Mao, T. Huang and A. Yu, *Int. J. Hydrogen Energy*, 2016, **41**, 13190–13196.
- 42 J. Wang, C. Liu, A. Lushington, N. Cheng, M. N. Banis, A. Riese and X. Sun, *Electrochim. Acta*, 2016, **210**, 285–292.
- 43 S.-H. Han, H.-M. Liu, J. Bai, X. L. Tian, B. Y. Xia, J.-H. Zeng, J.-X. Jiang and Y. Chen, *ACS Appl. Energy Mater.*, 2018, **1**, 3, 1252–1258.
- 44 S. G. d Silva, J. C. s M. Silva, G. S. Buzzo, A. O. Neto and M. H. M. T. Assumpcao, *Mater. Renewable Sustainable Energy*, 2016, **5**, 15, 14–21.
- 45 S. G. D. Silva, J. C. M. Silva, G. S. Buzzo, E. V. Spinacé, A. O. Neto and M. H. M. T. Assumpção, *Electrocatalysis*, 2015, **6**, 442–446.
- 46 Z. Li, F. Chen, W. Bian, B. Kou, Q. Wang, L. Guo, T. Jin, Q. Tang and B. Pan, *Electrochim. Acta*, 2021, **386**, 138465.
- 47 T. T. Gebremariam, F. Chen, B. Kou, L. Guo, B. Pan, Q. Wang, Z. Li and W. Bian, *Electrochim. Acta*, 2020, **354**, 136678.
- 48 M. G. Hosseini and R. Mahmoodi, *J. Power Sources*, 2017, **370**, 87–97.
- 49 S. Lai, C. Fu, Y. Chen, X. Yu, X. Lai, C. Ye and J. Hu, *J. Power Sources*, 2015, **274**, 604–610.
- 50 X. Zhang, W. Ooki, Y. R. Kosaka, A. Okonogi, G. Marzun, P. Wagener, S. Barcikowski, T. Kondo and J. Nakamura, *Appl. Surf. Sci.*, 2016, **389**, 911–915.
- 51 S.-S. Li, J.-J. Lv, L.-N. Teng, A.-J. Wang, J.-R. Chen and J.-J. Feng, *ACS Appl. Mater. Interfaces*, 2014, **6**, 13, 10549–10555.
- 52 W. S. Hummers and R. E. Offeman, *J. Am. Chem. Soc.*, 1958, **80**, 6, 1339.
- 53 A. Singh, M. Shirolkar, M. V. Limaye, S. Gokhale, C. Khan-Malek and S. K. Kulkarni, *Microsyst. Technol.*, 2013, **19**, 409–418.
- 54 G. J. Wang, Y. Z. Gao, Z. B. Wang, C. Y. Du, J. J. Wang and G. P. Yin, *J. Power Sources*, 2010, **195**, 185–189.
- 55 W. Su, Y. Fu, T. Wang, Y. Yu and J. Hu, *RSC Adv.*, 2015, **5**, 79178–79183.
- 56 S. S. A. E. Rehim, A. A. E. Basosi, S. M. E. Zein and M. M. Osman, *Collect. Czech. Chem. Commun.*, 1994, **59**, 2383–2389.
- 57 C. C. L. McCrory, S. Jung, J. C. Peters and T. F. Jaramillo, *J. Am. Chem. Soc.*, 2013, **135**, 1697.
- 58 M. G. Hosseini, V. Daneshvari-Esfahlan, S. Wolf and V. Hacker, *ACS Appl. Energy Mater.*, 2021, **4**, 6, 6025–6039.
- 59 R. Mahmoodi, M. G. Hosseini and H. Rasouli, *Appl. Catal., B*, 2019, **251**, 37–48.
- 60 D. Duan, X. You, J. Liang, S. Liu and Y. Wang, *Electrochim. Acta*, 2015, **176**, 1126–1135.
- 61 M. Zhang, Z. Yan and J. Xie, *Electrochim. Acta*, 2012, **77**, 237–343.
- 62 L. Zeng, Z. K. Tang and T. S. Zhao, *Appl. Energy*, 2014, **115**, 405–410.

- 63 S. G. D. Silva, J. C. M. Silva, G. S. Buzzo, A. O. Neto and M. H. M. T. Assumpcao, *Mater. Renewable Sustainable Energy*, 2016, **5**, 15–22.
- 64 M. Rezaei, S. H. Tabaian and D. F. Haghshenas, *Electrocatalysis*, 2014, **5**, 193–203.
- 65 T. Takamura and F. Mochimaru, *Electrochim. Acta*, 1969, **14**, 111–119.
- 66 M. G. Hosseini, M. M. Momeni and M. Faraji, *Electroanalysis*, 2010, **22**, 2620–2625.
- 67 G.-j Wang, Y.-z Gao, Z.-b Wang, C.-y Du, J.-j Wang and G.-p Yin, *J. Power Sources*, 2010, **195**, 185–189.
- 68 M. G. Hosseini and R. Mahmoodia, *New J. Chem.*, 2017, **41**, 13408–13417.
- 69 M. A. Dominguez-Crespo, E. Ramirez-Meneses, V. Montiel-Palma, A. M. T. Huerta and H. D. Rosales, *Int. J. Hydrogen Energy*, 2009, **34**, 1664–1676.
- 70 J. Ma and Y. Sahai, [Springer International Publishing Mater Struct, Cham](#), 2018, 249–283.
- 71 J. C. Calderón, M. R. Ráfales, M. J. Nieto-Monge, J. I. Pardo, R. Moliner and M. J. Lázaro, *Nanomaterials*, 2016, **6**, 187–205.
- 72 R. Mahmoodi, M. Chalani, M. G. Hosseini and M. Darbandi, *New J. Chem.*, 2020, **44**, 11974–11987.
- 73 K.-W. Park, J.-H. Choi, B.-K. Kwon, S.-A. Lee, Y.-E. Sung, H.-Y. Ha, S.-A. Hong, H. H. Kim and A. Wieckowski, *J. Phys. Chem. B*, 2002, **106**, 1869–1877.
- 74 J. Zhao, H. Li, Z. Liu, W. Hu, C. Zhao and D. Shi, *Carbon*, 2015, **87**, 116–127.
- 75 J. Florez-Montano, A. Calderon-Cardenas, W. Lizcano-Valbuena, J. L. Rodriguez and E. Pastor, *Int. J. Hydrogen Energy*, 2016, **16**, 19799–19809.
- 76 G. F. Lenz, R. Schneider, K. M. F. R. D. Aguiar, R. A. Bini, J. A. Chaker, P. Hammer, G. V. Botteselle, J. F. Felix and R. Schneider, *RSC Adv.*, 2019, **9**, 17157–17164
- 77 Y. Hu, F. He, A. Ben and C. Chen, *J. Electroanal. Chem.*, 2014, **726**, 55–61.
- 78 N. R. Council, C. O. C. Change, U. Transportation, T. R. Board, D. O. Earth and L. Studies, *Potential impacts of climate change on US transportation: Special report 290*, Transportation Research Board, 2008
- 79 A. M. Bartrom and J. L. Haan, *J. Power Sources*, 2012, **214**, 68–74.
- 80 Z. Liu, D. Ye, X. Zhu, S. Wang, R. Chen, Y. Yang and Q. Liao, *J. Power Sources*, 2021, **490**, 229553.
- 81 S. G. D. Silva, J. C. M. Silva, G. S. Buzzo, E. V. Spinace, A. O. Neto and M. H. M. T. Assumpcao, *Electrocatalysis*, 2015, **6**, 442–446.
- 82 Y. Li, Y. He and W. Yang, *J. Power Sources*, 2015, **278**, 569–573.
- 83 C.-M. Laia, J.-C. Lin, K.-L. Hsueh, C.-P. Hwang, K.-C. Tsay, L.-D. Tsai and Y.-M. Peng, *Int. J. Hydrogen Energy*, 2007, **32**, 4381–4388.

Footnotes

Queries and Answers

Q1

Query: Funder details have been incorporated in the funder table using information provided in the article text. Please check that the funder information in the table is correct and indicate any changes, if required. If changes are required, please ensure that you also amend the Acknowledgements text as appropriate.

Answer: The funder information is correct.

Q2

Query: Have all of the author names been spelled and formatted correctly? Names will be indexed and cited as shown on the proof, so these must be correct. No late corrections can be made.

Answer: Yes

Q3

Query: The Graphical Abstract text currently exceeds the space available for the published version. Please trim the text so that it is shorter than 250 characters (including spaces).

Answer: The text was shortened and became less than 250 characters as follow:

The obtained results show that the presence of Ni at the core instead of Co and using rGO as catalyst support instead of MWCNTs increased the catalytic performance of the synthesized electrocatalyst towards formate oxidation.

Q4

Query: Have all of the funders of your work been fully and accurately acknowledged? If not, please ensure you make appropriate changes to the Acknowledgements text.

Answer: Yes

Q5

Query: Ref. 2: Please provide the page (or article) number(s).

Answer: A. C. Staudt, *Bull. Am. Meteorol. Soc.*, 2008, **89**, 975–85.

Q6

Query: Ref. 70: Please provide the title.

Answer: J. Ma and Y. Sahai, *Anion Exchange Membrane Fuel Cells: Principles, Materials and Systems*, 2018, 249-283.